IEEE Access
Multidisciplinary | Rapid Review | Open Access Journal

Received December 3, 2019, accepted December 16, 2019, date of publication December 19, 2019, date of current version January 7, 2020.

Digital Object Identifier 10.1109/ACCESS.2019.2960871

An Adaptive Droop Control Strategy for Islanded Microgrid Based on Improved Particle Swarm Optimization

LIANG ZHANG[1], (Member, IEEE), HAO ZHENG[1], QUANGUI HU[2], BIN SU[2], AND LING LYU[1]

[1]School of Electrical Engineering, Northeast Electric Power University, Jilin 132012, China
[2]Beijing SGITG Accenture Information Technology Center Company, Ltd., Beijing 100031, China

Corresponding author: Liang Zhang (xiaozhanghit@163.com)

This work was supported in part by the National Natural Science Foundation of China, under Grant 51607031, in part by the Science and Technology Research Project of the 13th five-year Plan of Jilin Provincial Education Department, under Grant JJKH20180421KJ, and in part by the Jilin City Science and Technology Innovation Development Project, under Grant 20190104138.

ABSTRACT In an islanded microgrid with multiple distributed generations (DGs), the difference in line impedance may cause local voltage deviation, which leads to a series of problems such as lower power allocation accuracy and bus voltage drop under traditional droop control. In this respect, a method for optimizing the droop control using an improved particle swarm optimization (IPSO) is proposed. Firstly, the microgrid structure and influence of line parameters on traditional droop control strategy is analyzed. Then, an improved particle swarm optimization is proposed. Based on the basic particle swarm optimization (PSO) algorithm, a fuzzy inference system (FIS) is introduced to dynamically adjust the particle swarm optimization, which can effectively improve the global search ability and local search ability of the algorithm. After that, the improved algorithm is applied to the droop controller, simultaneously, the range of stable operation of the system is determined by small signal analysis. Finally, the simulation and experiment results show that the proposed improved droop control strategy can achieve accurate allocation of active and reactive power effectively while maintaining bus voltage and system frequency stability, enhance the dynamic performance and transient stability of the microgrid system.

INDEX TERMS Microgrid, fuzzy inference system, particle swarm optimization, droop control, power allocation.

I. INTRODUCTION

Microgrid is an effective way to give play to the effectiveness of distributed generation, which has great social and economic significance [1], [2]. The control mode of the microgrid is divided into master-slave and peer-to-peer control [3], [4]. Compared with the master-slave control, due to the simulation of the external characteristics of synchronous generator (SG) connected to the grid, the droop control strategy in the peer-to-peer control mode can automatically adjust the output power, which is easy to implement the plug-and-play of the distributed generation [5], [7].

However, due to the existence of line impedance and local load, the local information such as output voltage of each DG is not equal everywhere, resulting in insufficient power allocation accuracy and bus voltage drop [8], [9]. In response to the above problems, references [10]–[13] used the virtual impedance to feedback the output current to the voltage loop through a specific gain. After capturing the transient power change, the virtual impedance was adjusted to achieve accurate power allocation. However, the method increased the equivalent output impedance of the system, cannot guarantee the accuracy of the voltage control, and needed to obtain the line parameter information in advance. References [14]–[16] proposed an improved control strategy with network adaptive ability. By comparing the output information of DGs with the local information, the central control unit generated the required control variables and superimposed them into the local controller. Therefore, the output reference voltage of inverter was compensated to improve the accuracy of

The associate editor coordinating the review of this manuscript and approving it for publication was Amjad Anvari-Moghaddam.

This work is licensed under a Creative Commons Attribution 4.0 License. For more information, see http://creativecommons.org/licenses/by/4.0/

the system active power allocation. References [17], [18] proposed a compensation strategy for reactive power regulation, which maintained the bus voltage without affecting the power allocation accuracy and had strong robustness. However, in the above method, the interconnected communication line was used to provide local information. When communication delay occurs in the system, the accuracy of power allocation and the adaptability of control strategies cannot be guaranteed [19]. References [20]–[23] introduced the virtual synchronous generator (VSG) control technique. The results showed that the VSG control had greater inertia than the droop control and higher frequency stability. However, the power allocation accuracy of VSG control was greatly affected by the line parameters, and the active power in VSG control was more oscillating than the droop control strategy [24]. In order to solve the problem of unbalanced parallel output power of multiple energy storage batteries, references [25], [26] proposed a dynamic droop control strategy applying in the energy storage system (ESS), which dynamically allocated energy storage according to the state of charge (SOC) of the battery. However, it only optimized the consistency of the SOC, did not consider the proportional allocation of load power in the system.

At present, in the power system, the importance of artificial intelligence algorithms in solving complex problems has become increasingly prominent [27]. Compared with traditional control methods, it has unparalleled advantages, especially in the aspects of control, modeling, operation and analysis, which has become the main method to solve the problem of power system [28]. References [29]–[31] used the consistency algorithm and genetic algorithm (GA) to search for the optimal settings of key parameters in the microgrid, which not only improved the dynamic performance of the microgrid, but also can provide reference for the design of low voltage microgrid droop control parameters. However, the above method did not consider the influence of line impedance on DG, nor did it consider the power allocation of the system. References [32], [33] used the improved particle swarm optimization to optimize the parameters of the droop control in real time, which effectively improved the power allocation accuracy of the microgrid. However, as a centralized control structure, the above methods not only increase the complexity of the system, but also place high requirement on the communication system. References [34]–[37] improved the inertia weights and learning factors in the particle swarm optimization algorithm and realized the dynamic adjustment of parameters, which improved the convergence performance and search speed of the algorithm. However, due to the diversification of parameters in the algorithm, the above improvements still have certain oneness.

Therefore, this paper proposes a method to optimize the droop control using the improved particle swarm optimization algorithm. Firstly, the microgrid structure and the influence of line parameters on traditional droop control is analyzed. Then, an improved particle swarm optimization algorithm by introducing fuzzy inference system to adjust the learning factor and inertia weight of the algorithm is proposed. The improved particle swarm optimization algorithm is applied to the optimization process of the droop control afterwards. Finally, the simulation and experiment results show that the proposed improved droop control strategy can effectively improve the allocation accuracy of active and reactive power while maintaining the stability of voltage and frequency under different working conditions, and enhance the dynamic performance and stability of the microgrid.

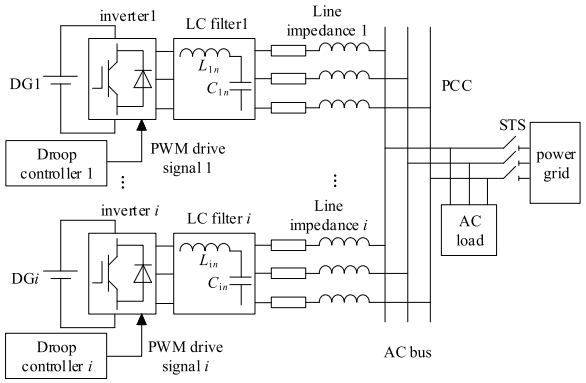

FIGURE 1. Topological structure diagram of multi-source microgrid.

The rest of this paper is organized as follows. Section II analyzes the network structure of the microgrid and the influence of line parameters on the traditional droop control. In section III, an improved particle swarm optimization algorithm is proposed and applied to the microgrid droop control. Section IV establishes the system small signal model and analyzes the stability of the system. In section V, the proposed control algorithm is simulated and verified. In section VI, the effectiveness of the proposed control algorithm is verified by experiments. Conclusions are drawn in Section VII.

II. MICROGRID STRUCTURE AND TRADITIONAL DROOP CONTROL

A. MICROGRID TOPOLOGICAL STRUCTURE

The microgrid topological structure when multiple distributed generations are connected in parallel is shown in Fig. 1.

As shown in Fig. 1, a total of *i* DG units are connected to the microgrid through an LC filter. For each DG unit, the power is provided by the renewable energy storage (RES) or ESS. To simplify the analysis process, this paper assumes a voltage source with a fixed direct current (DC) voltage connecting to the alternating current (AC) microgrid through an inverter. The load is connected to the point of common coupling (PCC), and the switching between the islanded and the grid-connected mode can be switched by breaking the static transfer switch (STS). In order to reflect the power allocation effectively and simplify the system as much as possible, this paper adopts the microgrid structure with double DG parallel operation.

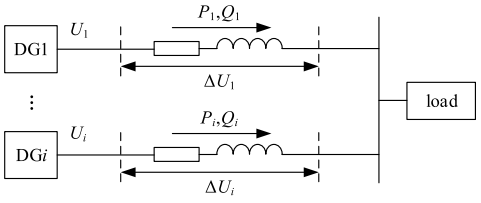

FIGURE 2. Simplified structure of microgrid.

B. THE PRINCIPLE AND SHORTCOMINGS OF TRADITIONAL DROOP CONTROL

From the topology of a microgrid with multiple DGs in Fig. 1, a simplified schematic of the microgrid can be obtained, as shown in Fig. 2 [17].

As shown in Fig. 2, the DG is connected to the microgrid through an inverter and an LC filter, and is connected to the AC bus through the line impedance to supply power to the load. Therefore, it can be concluded that the active and reactive power of each DG are:

$$P_i = \frac{U_i^2}{Z_i}\cos\theta_i - \frac{U_i U_{\mathrm{PCC}}}{Z_i}\cos(\theta_i + \delta_i) \tag{1}$$

$$Q_i = \frac{U_i^2}{Z_i}\sin\theta_i - \frac{U_i U_{\mathrm{PCC}}}{Z_i}\sin(\theta_i + \delta_i) \tag{2}$$

where U_i is the amplitude of the ith DG output voltage, U_{PCC} is the amplitude of the AC bus voltage, $Z_i\angle\theta_i$ is the line impedance from the ith DG to the AC bus, and δ_i is the phase difference between the phase of the ith DG output voltage and the PCC voltage.

Also, since $Ze^{j\theta} = Z\cos\theta + jZ\sin\theta = R + \mathrm{j}X$, equations (1) and (2) can be turned into:

$$P_i = \frac{1}{R_i^2 + X_i^2}(R_i U_i^2 - R_i U_i U_{\mathrm{PCC}}\cos\delta_i + X_i U_i U_{\mathrm{PCC}}\sin\delta_i) \tag{3}$$

$$Q_i = \frac{1}{R_i^2 + X_i^2}(X_i U_i^2 - XU_i U_{\mathrm{PCC}}\cos\delta_i + R_i U_i U_{\mathrm{PCC}}\sin\delta_i) \tag{4}$$

Assume $R << X$, the resistance portion of the line impedance can be ignored. Therefore, the active and reactive power of the ith DG output are:

$$P_i = \frac{U_i U_{\mathrm{PCC}}\sin\delta_i}{X_i} \tag{5}$$

$$Q_i = \frac{U_i U_{\mathrm{PCC}}\cos\delta_i - U_{\mathrm{PCC}}^2}{X_i} \tag{6}$$

Based on (5) and (6), it can be concluded that the active power P mainly depends on the voltage phase difference, and the reactive power Q mainly depends on the voltage amplitude. Therefore, P-f and Q-U can be described as droop characteristics shown in Fig. 3.

It can be concluded that the droop characteristic of microgrid is:

$$f = f^* - k_{\mathrm{P}}(P - P^*) \tag{7}$$

$$U = U^* - k_{\mathrm{Q}}(Q - Q^*) \tag{8}$$

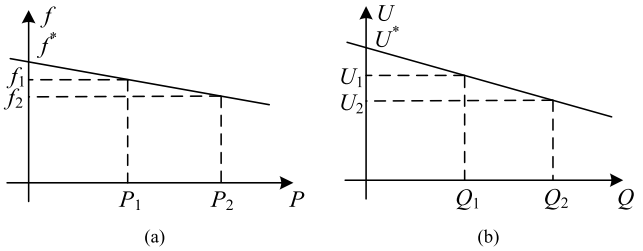

FIGURE 3. Droop characteristics of microgrid. (a) *P* - *f* droop characteristics. (b) *Q* - *U* droop characteristics.

where f is the frequency of the DG output voltage, f^* is the reference frequency of the microgrid system, U^* is the reference voltage of the microgrid system, k_{P} and k_{Q} are the frequency droop coefficient and the voltage droop coefficient in the droop control of the microgrid, respectively.

In the microgrid, frequency is a global variable of the system, and the corresponding active power of distributed generation can be allocated more accurately according to the droop curve. Since the output voltage of the DG is a local variable of the system, the corresponding reactive power cannot be allocated accurately by the traditional droop controller. Therefore, it is necessary to optimize the power allocation of the DG output.

According to the simplified microgrid in Fig. 2 we can conclude:

$$U_i = U_{\mathrm{PCC}} + \Delta U_i \tag{9}$$

$$\Delta U_i = \frac{X_i Q_i + R_i P_i}{U^*} \tag{10}$$

where ΔU_i is the voltage of the impedance of the ith line. As described above, since $R \ll X$, the line resistance is negligible:

$$\Delta U_i = \frac{X_i}{U^*}Q_i \tag{11}$$

It is assumed that the microgrid operates in parallel with double distributed generations and supplies power to the common load through PCC. According to (9) to (11), the reactive power characteristics of DG1 and DG2 can be obtained as follows:

$$U_1 = U_{\mathrm{PCC}} + \frac{X_1}{U^*}Q_1 = U_{\mathrm{PCC}} + k_1 Q_1 \tag{12}$$

$$U_2 = U_{\mathrm{PCC}} + \frac{X_2}{U^*}Q_2 = U_{\mathrm{PCC}} + k_2 Q_2 \tag{13}$$

where k_1, k_2 are the impedance coefficient of the DG1 and DG2 outlet line, respectively. Combining the droop characteristic curve described in (8), the reactive power allocation relationship when the double DGs connected in parallel is shown in Fig. 4.

As shown in Fig. 4, when the different line impedances are not equal, the steady-state operating point of the microgrid is located at two points A and B. It is assumed that the reactive power gains of the two DGs are the same, when the line impedance $X_1 < X_2$, there is $Q_1 > Q_2$, therefore, the reactive

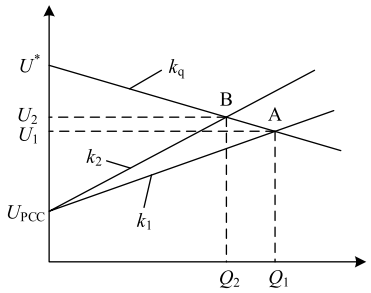

FIGURE 4. Reactive power allocation relationship.

power cannot be allocated accurately when DG1 and DG2 are connected in parallel.

III. IMPROVED PARTICLE SWARM OPTIMIZATION

A. BASIC PARTICLE SWARM OPTIMIZATION

The PSO algorithm is initialized to a group of random particles (random solutions) to find the optimal solution through iteration. In the optimization process, particles update themselves with two extreme value in each iteration: the one is the optimal solution found by the particle itself, called the individual extremum; another extreme value is found by the entire population, called the global extremum [38].

In the d-dimensional target search space, there are n particles forming a group. When the above two extreme values are found, the particles update their speed and position according to the following formula [39]:

$$v_{id} = \omega \times v_{id} + c_1 r_1 (p_{id} - x_{id}) + c_2 r_2 (p_{gd} - x_{id}) \quad (14)$$

$$x_{id} = x_{id} + v_{id} \quad (15)$$

where c_1 and c_2 are learning factors, also called acceleration constants; r_1 and r_2 are uniform random numbers in [0,1]; ω is the inertia weight, which keeps the particles in motion inertia and has the ability to expand the search space.

B. FUZZY RULE SYSTEM

Although the basic PSO is easy to implement, when it is based on the droop control strategy to optimize the complex nonlinear microgrid, it has the disadvantage of being easily trapped in local optimum and insufficient detection capability. Based on the analysis of the introduction in this paper, in order to improve the search speed and accuracy of the PSO, this paper improves the basic PSO by adjusting the learning factors c_1, c_2 and inertia weight ω dynamically through fuzzy inference system (FIS) [37]. This paper calculates the performance measures of the algorithm, such as the diversity of particles, the error of a certain point in the algorithm execution, and the iteration itself, as the basis for adjusting the algorithm parameters, which are dynamically changed in each iteration of the algorithm.

For measuring the iterations of the algorithm, it is used the ratio of the number of current iterations to the maximum number of iterations of each particle, and the value is between 0 and 1. When the algorithm is running initially, *Iteration* approaches 0. As the number of iterations increases, *Iteration* increases and approaches 1 gradually. The calculation formula is:

$$Iteration = \frac{Current\ Iteration}{Maximum\ of\ Iterations} \quad (16)$$

The diversity measure is defined by (17), which measures the degree of dispersion of the particles. That is, when the particles are close together, *Diversity* is small, and when the particles are separated, *Diversity* is high. The diversity equation can be thought of as the average of the Euclidean distance between each particle and the best particle.

$$Diversity = \frac{1}{n_s} \sum_{i=1}^{n_s} \sqrt{\sum_{j=1}^{n_x} \left(x_{ij}(t) - \overline{x_j}(t)\right)^2} \quad (17)$$

The error measure is defined by the (18). The difference between the population and the optimal particle is measured by averaging the difference between the fitness of each particle and optimal particle. When the convergence effect of the algorithm is better, the particle approaches the global optimal solution, *Error* is larger, conversely, *Error* is smaller.

$$Error = \frac{1}{n_s} \sum_{i=1}^{n_s} (F(x_i) - F(x_i)_{\min}) \quad (18)$$

Therefore, for designing the fuzzy systems, the three measurements described above were considered as inputs. Since the input of the fuzzy system has a defined range of values from 0 to 1 (0% to 100%), *Diversity* and *Error* need to be normalized to meet the defined range. Equations (19) and (20) show that how *Diversity* and *Error* are normalized, respectively.

$$Diversity_n = \begin{cases} 0, & \lambda_{\min} = \lambda_{\max} \\ \dfrac{\lambda - \lambda_{\min}}{\lambda_{\max} - \lambda_{\min}}, & \lambda_{\min} \neq \lambda_{\max} \end{cases} \quad (19)$$

The *Diversity* normalization process is shown in (19). To simplify the expression, *Diversity* is expressed as λ. The first condition is that the maximum Euclidean distance is equal to the minimum Euclidean distance, which means that the particles are just in the same position, so there is no diversity. The second condition deals with situations with different Euclidean distances.

$$Error_n = \begin{cases} 1, & F_{\min} = F_{\max} \\ \dfrac{\varepsilon - F_{\min}}{F_{\max} - F_{\min}}, & F_{\min} \neq F_{\max} \end{cases} \quad (20)$$

The *Error* normalization process is shown in (20). To simplify the expression, *Error* is expressed as ε. The first condition shows that when the minimum fitness is equal to the maximum fitness, $Error_n$ will be 1 because the particles are close to each other. The second condition is to deal with the situations where the suitability is different.

According to the above analysis, a FIS with 3 inputs, 3 outputs, and 27 rules can be established. The input is *Iteration*, $Diversity_n$, and $Error_n$, the output is the learning

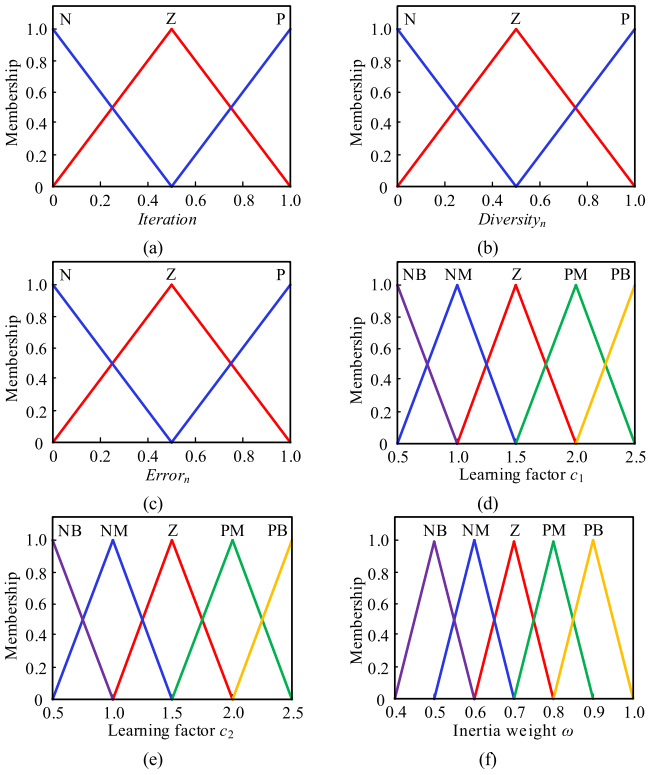

FIGURE 5. Fuzzy inference system membership function. (a) *Iteration* membership function. (b) *Diversity*$_n$ membership function. (c) *Error*$_n$ membership function. (d) Learning factor c_1 membership function. (e) Learning factor c_2 membership function. (f) Inertia weight ω membership function.

TABLE 1. Fuzzy logic rule tables.

Number	λ	γ	ε	ω	c_1	c_2
1	N	N	N	PB	NB	NM
2	N	N	Z	PM	Z	Z
3	N	N	P	PM	NM	NB
4	N	Z	N	PM	Z	Z
5	N	Z	Z	PM	PM	NM
6	N	Z	P	Z	PM	NB
7	N	P	N	PM	NM	NB
8	N	P	Z	Z	PM	NB
9	N	P	P	NM	PB	NB
10	Z	N	N	PM	NB	NM
11	Z	N	Z	PM	NM	PM
12	Z	N	P	Z	Z	Z
13	Z	Z	N	PM	NM	PM
14	Z	Z	Z	Z	Z	Z
15	Z	Z	P	NM	PM	NM
16	Z	P	N	Z	Z	Z
17	Z	P	Z	NM	PM	NM
18	Z	P	P	NM	PM	NB
19	P	N	N	PM	NB	PB
20	P	N	Z	Z	NB	PM
21	P	N	P	NM	NB	NM
22	P	Z	N	Z	NB	PM
23	P	Z	Z	NM	NM	PM
24	P	Z	P	NM	Z	Z
25	P	P	N	NM	NB	NM
26	P	P	Z	NM	Z	Z
27	P	P	P	NB	NM	NB

factor c_1, c_2, and the inertia weight ω of the particle swarm algorithm. First, the domain of input and output should be determined, and the parameters should be controlled according to experience in a reasonable range. Therefore, the setting domain of *Iteration*, *Diversity*$_n$, and *Error*$_n$ is set to [0, 1], the domain of inertia weight ω is [0.4, 1], and the domain of learning factors c_1 and c_2 is [0.5, 2.5]. Secondly, since the above parameters only need fine adjustment, in order to reduce the number of fuzzy logic rules and simplify the optimization process, the number of input fuzzy partitions is set to three [32], which are ''negative (N)'', ''zero (Z)'', and ''positive (P)''. The number of output fuzzy partitions is five, which are ''negative large (NB)'', ''negative medium (NM)'', ''zero (Z)'', ''medium (PM)'', and ''positive (PB)''. The FIS adopts the Mamdani type system, and the defuzzification uses the centroid center of gravity method. In addition, since the triangular membership function is simple and commonly used, also the optimization effect is good [40], this paper uses the triangular membership function, as shown in Fig. 5.

The introduction of FIS to optimize PSO algorithm should satisfy the following two aspects: in the initial stage of algorithm running, the distance between particle and optimal solution is large, *Iteration*, *Diversity*$_n$, and *Error*$_n$ are small, the global search ability of the algorithm should be improved; in the later stage of algorithm running, the distance between the particle and the optimal solution is small, *Iteration*, *Diversity*$_n$, and *Error*$_n$ are large, and the local search ability of the algorithm should be improved. According to the above principles, the fuzzy logic rules are shown in Table 1 [37].

C. FITNESS FUNCTION AND OPTIMIZATION PROCESS

Considering the proportional allocation of active and reactive power, bus voltage fluctuation and frequency oscillation, this paper designs a fitness function for IPSO proposed above. Since the output power of the DG is inversely proportional to the droop coefficient [41], [42], the algorithm can be used to appropriately adjust the droop coefficient in order to reasonably allocate power according to the DG capacity.

The fitness function of the IPSO algorithm is:

$$F_i = \Delta P_i + \Delta Q_i + \Delta U_i + \Delta f_i \tag{21}$$

Among them, the power deviation of DGi calculation formula is:

$$\Delta P_i = \frac{\left|P_i - P_i^*\right|}{P_i^*} \tag{22}$$

$$\Delta Q_i = \frac{\left|Q_i - Q_i^*\right|}{Q_i^*} \tag{23}$$

Among them, P_i and Q_i is the active and reactive power of DGi, respectively. P_i^* and Q_i^* are the reference active and reactive power of DGi, respectively, as shown in the following equation.

$$P_i^* = \frac{c_i}{c_{total}} \sum_{i=1}^{n} P_i$$
$$Q_i^* = \frac{c_i}{c_{total}} \sum_{i=1}^{n} Q_i$$

where c_{i} and c_{total} are the capacity of the DGi and the total DG of the system, respectively.

The voltage deviation calculation formula is:

$$\Delta U_i = \frac{|U_i - U^*|}{U^*} \tag{24}$$

where U_i is the output voltage of DGi, U^* is the rated voltage of the system.

The frequency deviation calculation formula is:

$$\Delta f_i = \frac{|f_i - f^*|}{f^*} \tag{25}$$

where f_i is the frequency of output voltage of DGi, f^* is the rated frequency of 50 Hz.

The particle dimension of the algorithm is set to two-dimensions, which represents the active and reactive droop coefficients respectively in each droop controller. According to the fuzzy rules and fitness function, the optimized droop control flow of the IPSO algorithm proposed in this paper is shown in Fig. 6.

D. CONTROL STRUCTURE AND COMMUNICATION MECHANISM

Apply the IPSO algorithm proposed above to the droop controller, the control structure is shown in Fig. 7. Among them, there is a DG operating in the microgrid, and the droop controller provides a control signal for the inverter. Using this control strategy, the IPSO module and the droop control module realize real-time interaction between different information.

Since the improved droop control structure designed in this paper requires global and local information to be transmitted between different DGs, it is necessary to establish the corresponding communication mechanism. In order to simplify the structure of the controller, reduce the amount of calculation, and improve the control efficiency, the method uses the central controller to receive local information including the instantaneous power, voltage, and other information of each DG unit, and periodically send it to the local inverter, the deviation calculation module in the local controller generates the deviation value of each variable, which are directly input into the IPSO module. Then, the IPSO enters a new optimization cycle and analyzes the deviation information of the control variables. After the FIS is used to adjust the algorithm parameters, the corresponding fitness function is calculated and the particle is updated to complete the first

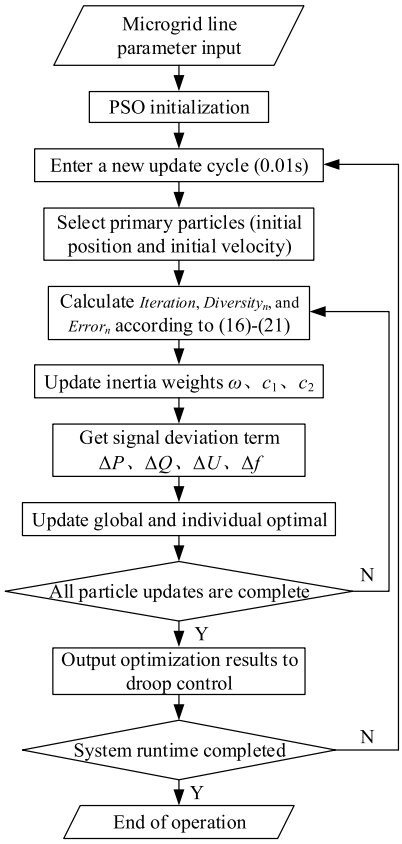

FIGURE 6. Fuzzy inference system membership function.

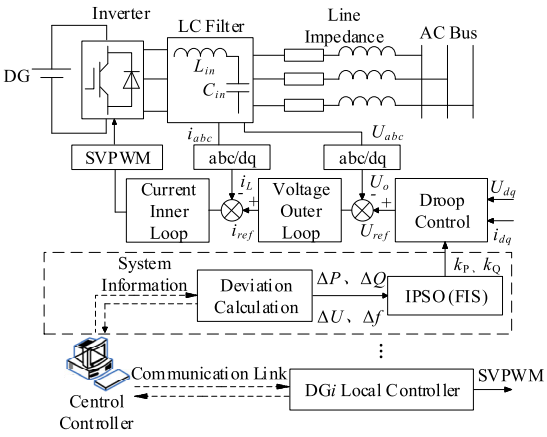

FIGURE 7. Microgrid control structure diagram based on improved control strategy.

cycle, and the next update is determined according to the judgment condition. Finally, the obtained two-dimensional extreme values k_{P} and k_{Q} are input into the droop control module in real time, and the original droop coefficient is updated. The signal reference value remains constant during the update interval period. When the local controller receives the updated the signal deviation sent by the central controller, this means that a new round of optimization process has begun. The central controller continues to calculate the power reference and sends this value periodically (10 ms in

the method). When the communication signal is lost due to interference, if the load demand does not change, the power allocation will remain unchanged. Once the load changes, it will cause a deviation in the reference voltage and power in the microgrid. Due to the improved droop control and the voltage compensation already generated, the offset value is smaller than the conventional droop controller.

IV. SMALL SIGNAL STABILITY ANALYSIS

Because the studied microgrid system is a non-linear system, the structure of the DG in parallel makes the system more complicated, and there are many parameters can affect the stability of the system, this paper will establish and analyze the small signal model of the system by linearizing near the static operating point [43]. It can be seen from the analysis in the previous section that the active power and reactive power output by the inverter can be expressed in the form of (3) and (4), respectively, and the droop characteristic curve can be expressed in the form of (7) and (8). Assuming that the steady-state operating point of the system is (δ_0, E_0, U_0), then the linearization model of (3), (4) and (7), (8) after considering small signal perturbations is:

$$\begin{cases} \Delta\omega = \dfrac{\partial\omega}{\partial P}\Delta P \\ \Delta E = \dfrac{\partial E}{\partial Q}\Delta Q \\ \Delta P = \dfrac{\partial P}{\partial E}\Delta E + \dfrac{\partial P}{\partial \delta}\Delta\delta \\ \Delta Q = \dfrac{\partial Q}{\partial E}\Delta E + \dfrac{\partial Q}{\partial \delta}\Delta\delta \end{cases} \tag{26}$$

where Δ is the small signal deviation of the steady state operating point. Substituting (3) into (6) and calculating the partial derivative, it can be obtained:

$$\begin{cases} \Delta\omega = -k_{\mathrm{P}}\Delta P \\ \Delta E = -k_{\mathrm{Q}}\Delta Q \\ \Delta P = k_{\mathrm{Pe}}\Delta E + k_{\mathrm{Pd}}\Delta\delta \\ \Delta Q = k_{\mathrm{Qe}}\Delta E + k_{\mathrm{Qd}}\Delta\delta \end{cases} \tag{27}$$

In the above equations:

$$\begin{aligned} k_{\mathrm{Pe}} &= \frac{1}{R^2+X^2}(2RE_{\mathrm{e}} - RU_{\mathrm{e}}\cos\delta_{\mathrm{e}} + XU_{\mathrm{e}}\sin\delta_{\mathrm{e}}) \\ k_{\mathrm{Pd}} &= \frac{1}{R^2+X^2}(RE_{\mathrm{e}}U_{\mathrm{e}}\sin\delta_{\mathrm{e}} + XE_{\mathrm{e}}U_{\mathrm{e}}\cos\delta_{\mathrm{e}}) \\ k_{\mathrm{Qe}} &= \frac{1}{R^2+X^2}(2RE_{\mathrm{e}} - XU_{\mathrm{e}}\cos\delta_{\mathrm{e}} + RU_{\mathrm{e}}\sin\delta_{\mathrm{e}}) \\ k_{\mathrm{Qd}} &= \frac{1}{R^2+X^2}(XE_{\mathrm{e}}U_{\mathrm{e}}\sin\delta_{\mathrm{e}} + RE_{\mathrm{e}}U_{\mathrm{e}}\cos\delta_{\mathrm{e}}) \end{aligned}$$

Since the droop control is used in this paper, it is necessary to measure and obtain the output active and reactive power value. Generally, the measured power is filtered through a low-pass first order filter to filter out the high-frequency components in the instantaneous power [44], so the detected power is passed through a low-pass first order filter $\omega_{\mathrm{c}}/(s+\omega_{\mathrm{c}})$, combined (7) available:

$$\Delta\omega(s) = -\frac{k_{\mathrm{P}}\omega_{\mathrm{c}}}{s+\omega_{\mathrm{c}}}(k_{\mathrm{Pe}}\Delta E(s) + k_{\mathrm{Pd}}\Delta\delta(s)) \tag{28}$$

$$\Delta E(s) = -\frac{k_{\mathrm{Q}}\omega_{\mathrm{c}}}{s+\omega_{\mathrm{c}}}\left(k_{\mathrm{Qe}}\Delta E(s) + k_{\mathrm{Qd}}\Delta\delta(s)\right) \tag{29}$$

Since $\Delta\omega(s) = s\Delta\delta(s)$, substituting it into (25), (29), it can be obtained:

$$s^3\Delta\delta(s) + as^2\Delta\delta(s) + bs\Delta\delta(s) + c\Delta\delta(s) = 0 \tag{30}$$

In the above equations:

$$\begin{aligned} a &= (2 + k_{\mathrm{Q}}k_{\mathrm{Qe}})\omega_{\mathrm{c}} \\ b &= (k_{\mathrm{P}}k_{\mathrm{Pd}} + k_{\mathrm{Q}}k_{\mathrm{Qe}}\omega_{\mathrm{c}} + \omega_{\mathrm{c}})\omega_{\mathrm{c}} \\ c &= (k_{\mathrm{Pd}} + k_{\mathrm{Q}}k_{\mathrm{Pd}}k_{\mathrm{Qe}} - k_{\mathrm{Q}}k_{\mathrm{Pe}}k_{\mathrm{Qd}})k_{\mathrm{P}}\omega_{\mathrm{c}}^2 \end{aligned}$$

Equation (30) is homogeneous and the free motion system can be described as a small signal disturbance model based on the steady state operating point (δ_0, E_0, U_0), therefore, the response of the system can be obtained by the following equation:

$$\lambda^3 + a\lambda^2 + b\lambda + c = 0 \tag{31}$$

where a, b, and c are the same with (30).

Based on (31), the stability of the proposed controller can be analyzed by using the root locus plots method. When $\delta = 0.0643$, $U = 225$ V, $U_{\mathrm{PCC}} = 220$ V, $Z = 0.642 + \mathrm{j}2.64\times10^{-4}\Omega$, $k_{\mathrm{P}} = 2\times10^{-4}$, and $k_{\mathrm{Q}} = 1\times10^{-5}$ is a steady-state operating point of the system. Based on the steady-state operating point, this paper will analyze the influence of system parameter changes on system stability.

When the other parameters maintain a certain value, the root locus plot when X is changed within the range of 0 to 5 Ω is shown in Fig. 8 (a). It can be seen from the figure that as the value of X increases, the imaginary parts of the two conjugate virtual roots tend to zero, and the system exhibits strong damping characteristics, which increases the response time of the system. When X is too small or too large, there is a feature root that will gradually approach the imaginary axis, affecting the stability of the system.

When the other parameters maintain a certain value, the root locus plot when R changes within the range of 0.01 to 10 Ω is shown in Fig. 8 (b). It can be seen from the figure that as the R value increases, the imaginary parts of the two conjugate virtual roots tend to zero, and the system exhibits strong damping characteristics, which increases the response time of the system. When R is too large, a characteristic root will gradually approach the imaginary axis, affecting the stability of the system.

When the other parameters maintain a certain value, the root locus plot when the droop coefficients k_{P} and k_{Q} are changed within the range of 1×10^{-4} to 0.1 and 0.5×10^{-5} to 0.1, respectively, as shown in Fig. 8 (c) and (d). It can be seen from the figure that as k_{P} and k_{Q} increases, the real part of the eigenvalue becomes larger and larger, indicating that the

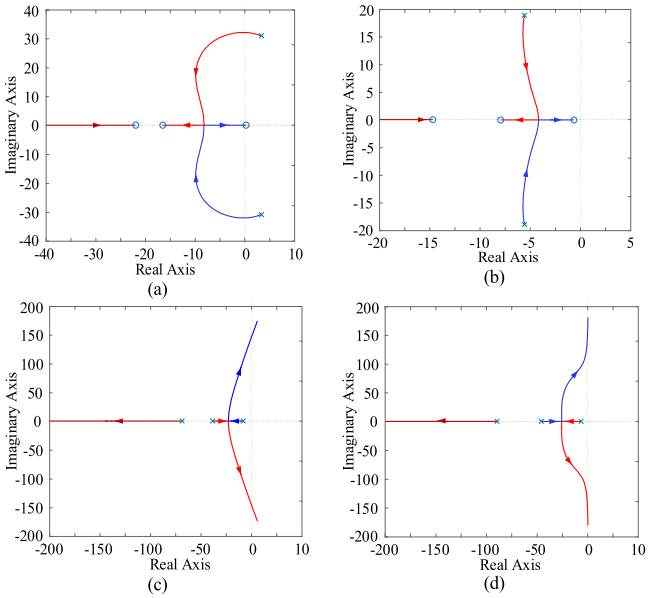

FIGURE 8. System root locus map when parameters change. (a) System root locus map when X changes. (b) System root locus map when R changes. (c) System root locus map when k_P changes. (d) System root locus map when k_Q changes.

stability of the system is decreasing, that is, the larger the k_P and k_Q, the weaker the stability of the system.

According to the analysis, in order to ensure the stability of the microgrid, the reactance of the line parameters ranges from 0.1 to 5 Ω, the resistance ranges from 1.12×10^{-5} to 6.32×10^{-2} Ω, and the active and reactive powers in the algorithm are set. The optimization range of the droop coefficient is 1×10^{-4} to 0.5×10^{-2} and 0.5×10^{-5} to 0.5×10^{-3}, respectively.

V. SIMULATION RESULTS

A. ALGORITHM EVALUATION

In order to test the performance of the proposed IPSO algorithm, This paper uses several types of classic fitness functions to simulate the proposed algorithm, including many local minima, plate-shaped, valley-shaped, steep ridges/drops, and other types of fitness functions, as shown in Table 2 [28], where d is the dimension of the algorithm optimization. Based on the classical fitness function, the basic PSO, the AWPSO proposed in [36] and the IPSO proposed in this paper are simulated in this section.

The parameters of the algorithm used in this simulation are shown in Table 3.

Since the global minimum and maximum values of each test function are not same, for the comparison, the optimization result of each function is normalized, as shown in (8), and the final result is between 0 and 1. The closer the search result is to zero, the higher the accuracy of the algorithm, and the opposite is true. Therefore, this value reflects the difference between the experimental results and the global optimal values [37].

$$g_{norm} = \left| \frac{g_i - g_{best}}{g_{\max} - g_{best}} \right| \tag{32}$$

TABLE 2. Simulation parameter setting.

Function	Name	Definition
f_1	Sphere	$f(x)=\sum_{i=1}^{d} x_i^2$
f_2	Rotated Hyper-Ellipsoid	$f(x)=\sum_{i=1}^{d}\sum_{j=1}^{i} x_j^2$
f_3	Rosenbrock	$f(x)=\sum_{i=1}^{d-1}\left[100(x_{i+1}-x_i^2)^2+(x_i-1)^2\right]$
f_4	Rastrigin	$f(x)=10d+\sum_{i=1}^{d}\left[x_i^2-10\cos(2\pi x_i)\right]$
f_5	Griewank	$f(x)=\sum_{i=1}^{d}\frac{x_i^2}{4000}-\prod_{i=1}^{d}\left(\frac{x_i}{\sqrt{i}}\right)+1$
f_6	Michalewicz	$f(x)=-\sum_{i=1}^{d}\sin(x_i)\sin^{2m}\left(\frac{ix_i^2}{\pi}\right)$
f_7	Styblinski-Tang	$f(x)=\frac{1}{2}\sum_{i=1}^{d}(x_i^4-16x_i^2+5x_i)$
f_8	Trid	$f(x)=\sum_{i=1}^{d}(x_i-1)^2-\sum_{i=2}^{d}x_i x_{i-1}$
f_9	Zakharov	$f(x)=\sum_{i=1}^{d}x_i^2+\left(\sum_{i=1}^{d}0.5ix_x\right)^2+\left(\sum_{i=1}^{d}0.5ix_x\right)^4$
f_{10}	Schwefel	$f(x)=418.9829d-\sum_{i=1}^{d}x_i(\sqrt{\lvert x_i\rvert})$

TABLE 3. Simulation parameters setting.

Parameter	PSO	AWPSO	IPSO
Population	10	10	10
Iterations	30	30	30
c_1	2	2	dynamic
c_2	2	2	dynamic
ω	0.5	dynamic	dynamic

where g_{norm} is the algorithm optimization result after normalization, g_i is the optimization result of the algorithm under the ith fitness function, g_{best} and g_{max} are the global optimal value and the maximum value of the ith fitness function, respectively. Since the proposed algorithm is applied to the update of active and reactive droop coefficients, the two-dimensional test function is selected to verify the algorithm, ie., $d = 2$. Combined with the value range of each fitness function independent variable and the function image, the maximum value of the function can be obtained. Therefore, the experimental results of each method and each function can be obtained, as shown in Table 4.

It can be seen from the simulation results in Table 4 that the IPSO algorithm proposed in this paper can accurately converge to the global optimal solution at a faster speed under various types of fitness functions. Compared with AWPSO and basic PSO, it has obvious advantages and can be effectively applied to the microgrid droop controller to realize real-time optimization of power, voltage and frequency in the system.

TABLE 4. Simulation parameter setting.

Function	Maximum	Minimum	PSO	AWPSO	IPSO
f_1	52.43	0	0.0000	0.0000	0.0003
f_2	12884.90	0	0.0000	0.0001	0.0003
f_3	168136.00	0	0.0000	0.0004	0.0008
f_4	78.93	0	0.0002	0.0025	0.0118
f_5	2.18	0	0.0002	0.0013	0.0085
f_6	-0.36	-1.8013	0.0001	0.0008	0.0015
f_7	250.00	-78.33	0.0002	0.0012	0.0028
f_8	32.54	-2	0.0002	0.0024	0.0103
f_9	48022.36	0	0.0000	0.0006	0.0063
f_{10}	1413.52	0	0.0000	0.0062	0.0148

TABLE 5. Simulation parameter setting.

Symbol	Parameters	Values
U_{dc}	DC voltage source	700 V
L	Filter inductor	1.5 mH
C	Filter capacitor	20 μF
R_{line1}	DG1 line impedance	$0.642+j2.64\times10^{-4}$ Ω
R_{line2}	DG2 line impedance	$0.321+j1.32\times10^{-4}$ Ω
U_{PCC}	Bus voltage rms	220 V
f	System frequency	50 Hz
k_P	Initial active power droop coefficient	2×10^{-4}
k_Q	Initial reactive power droop coefficient	1×10^{-5}

B. SIMULATION ANALYSIS

In this section, the simulation of the microgrid operation of two DGs connected in parallel is carried out. The capacity ratio of DG1 and DG2 is set to 2:1, namely, the power allocation ratio of DG1 and DG2 is 2:1. In addition, with reference to the IEEE Std 1547^{TM}-2018 standard, the thresholds for setting the frequency deviation Δf (Hz) and the voltage deviation ΔU (%) are 0.3 Hz and 10%, respectively [45], and exceeding the threshold is considered to enter the unstable interval. According to the value range of the parameters during the stable operation of the system obtained by small signal analysis, the simulation parameters are shown in Table 5.

1) UNBALANCED CONDITION UNDER CONSTANT POWER LOAD

In this section, the strategy proposed in this paper is verified under the conditions of constant power load switching. Among them, the public load is a constant power load, and the system parameter settings are shown in Table 5. At $t = 1.3$ s, the active load increases by 5 kW and the reactive load increases by 2 kvar. At $t = 1.6$ s, the active load is reduced by 2 kW and the reactive load is reduced by 2 kvar. Fig. 9 shows the simulation results of the improved control strategy proposed in this paper.

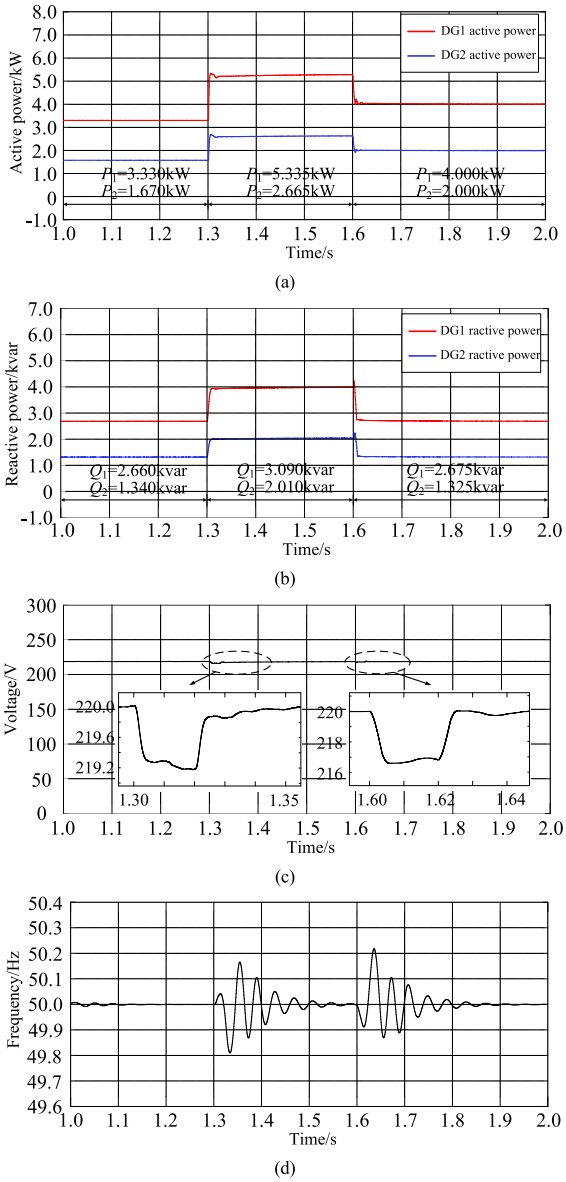

FIGURE 9. Simulation results under improved droop control strategy when the constant power load switching. (a) DGs active power. (b) DGs reactive power. (c) Bus voltage rms. (d) System frequency.

It can be seen from Fig. 9 that the constant power load is stable after startup, and when the active and reactive loads increase or decrease at the same time, the output power of the two DGs can be quickly and accurately allocated according to their power capacity. In this process, the voltage drop is up to 3 V, which can be restored to the rated voltage after 0.05 s. The maximum frequency fluctuation is 0.2 Hz, which remains stable after oscillating for 0.2 s.

Under the same parameter setting conditions, the system is simulated under the traditional droop control strategy, and the power allocation error, voltage and frequency deviation of the traditional improved droop control strategy under constant power load are calculated, as shown in Table 6 and Table 7. As can be seen from the data in the table, the traditional droop

TABLE 6. Comparison of power allocation error between traditional and improved strategy under constant power load.

Operation time / s	Active power allocation error / %		Reactive power allocation error / %	
	Traditional	Improved	Traditional	Improved
1.0-1.3	3.63	0.09	8.62	0.23
1.3-1.6	5.16	0.37	12.35	3.00
1.6-2.0	3.21	0	9.81	0.34

TABLE 7. Comparison of stability index error between traditional and improved strategy under constant power load.

Operation time / s	Frequency fluctuation Δf / Hz		Voltage fluctuation ΔU / %	
	Traditional	Improved	Traditional	Improved
1.0-1.3	0	0	0	0
1.3-1.6	0.30	0.20	1.5	0.3
1.6-2.0	0.35	0.20	2.4	3.1

control cannot achieve power allocation, although the voltage and frequency comply with the IEEE Std 1547^{TM}-2018 standard mentioned above, there is still room for improvement. In contrast, the improved strategy proposed in this paper can effectively improve power allocation accuracy and voltage deviation.

2) UNBALANCED CONDITION UNDER MOTOR LOAD

In fact, motor load occupies a large proportion in power systems [46]. Because the motor load has high requirements on the line impedance imbalance, and the control process is difficult compared with the ordinary load [47], this section uses the motor load as an example to verify the method proposed in this paper. The system parameter settings, load switching time, and load capacity are the same as in the previous section.

It can be seen from Fig. 10 that the motor load is in a steady state after starting, and when the active and reactive loads are simultaneously increased or decreased, the power supply capacity quickly allocates the power of two DG units with high accuracy. In the process, the voltage drop is up to 7 V, and the amplitude can be restored to 220 V after 0.1 s amplitude. The maximum frequency fluctuation is 0.25 Hz, which is stable after 0.2 s oscillation.

Under the same parameter setting conditions, the system is simulated under the traditional droop control strategy, and the power allocation errors, voltage and frequency deviations of the traditional and improved droop control strategies under motor loads are calculated, as shown in Table 8 and Table 9. It can be seen from the data in the table that the traditional droop control fails the power allocation, and the voltage and frequency fluctuate greatly compared to the improved strategy proposed in this paper, and there is a serious voltage sag, which does not satisfy the IEEE Std 1547^{TM}-2018 standard. The improved droop control strategy realizes the rapid differential allocation of power, and suppresses the fluctuation of voltage and frequency within the specified range, which

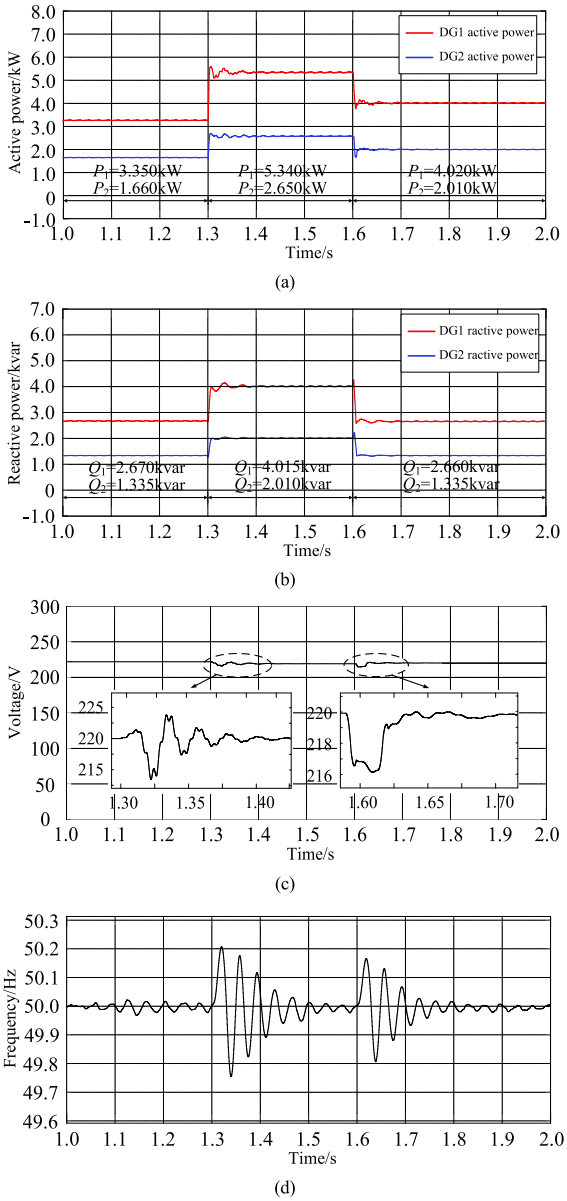

FIGURE 10. Simulation results under improved droop control strategy when motor load switching. (a) DGs active power. (b) DGs reactive power. (c) Bus voltage rms. (d) System frequency.

TABLE 8. Comparison of power allocation error between traditional and improved strategy under motor load.

Operation time / s	Active power allocation error / %		Reactive power allocation error / %	
	Traditional	Improved	Traditional	Improved
1.0-1.3	8.80	0.51	21.00	0.15
1.3-1.6	6.75	0.13	13.30	0.38
1.6-2.0	7.00	0.50	20.00	0.23

significantly improves the stability of the system compared with the traditional method.

3) MUTATION OF LINE PARAMETERS

This example verifies the condition in which the system line parameters are abrupt. In this case, the common load is motor

TABLE 9. Comparison of stability index error between traditional and improved strategy under motor load.

Operation time / s	Frequency fluctuation Δf / Hz		Voltage fluctuation ΔU / %	
	Traditional	Improved	Traditional	Improved
1.0-1.3	0	0	0	0
1.3-1.6	0.50	0.20	4.5	2.8
1.6-2.0	0.43	0.22	5.1	1.7

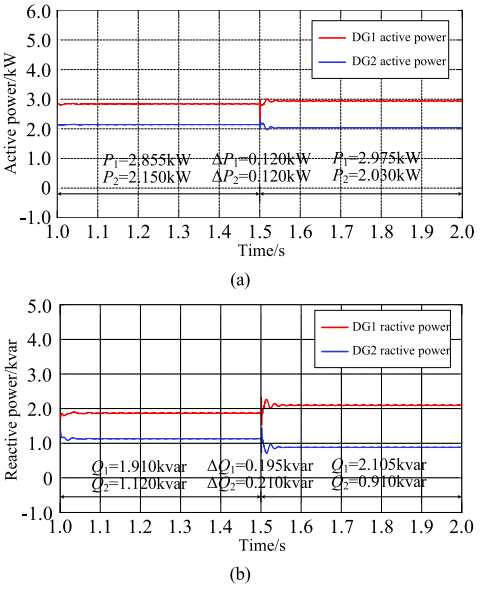

FIGURE 11. Simulation results under traditional droop control strategy when line parameters suddenly change. (a) DGs active power. (b) DGs reactive power.

load, and the active load is set to 5 kW, and the reactive load is 3 kvar. According to the range of line impedance obtained in the small signal analysis above, the impedance of DG2 line changes from $0.321+\mathrm{j}1.32\times10^{-4}$ Ω to $1.284+\mathrm{j}1.0\times10^{-3}$ Ω at $t = 1.5$ s, and the DG1 line parameters remain unchanged.

It can be seen from Fig. 11 that when the system line parameters are abrupt, the deviation of the active and reactive power between two DGs is more obvious under the traditional droop control. In Fig. 12, the improved droop control strategy proposed in this paper can re-divide active and reactive power, and significantly reduce the impact of line parameter abrupt changes on power allocation accuracy. Table 10 shows the power deviation percentage before and after the sudden change of the line parameters under the two control methods. It can be concluded that the control algorithm proposed in this paper is suitable for the operation of the line parameter mutation.

4) PLUG-AND-PLAY FUNCTIONALITY

Plug-and-play is the basic function of a microgrid system with multiple DG units. Fig. 13 shows the simulation results using the proposed control strategy when DG2 fails. At the beginning of the simulation, the system operates under the

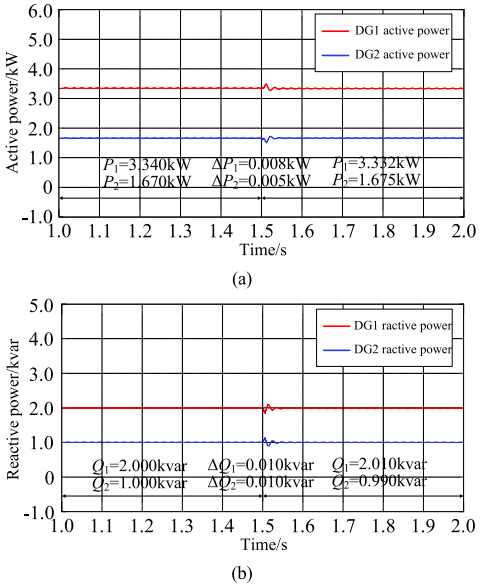

FIGURE 12. Simulation results under improved droop control strategy when line parameters suddenly change. (a) DGs active power. (b) DGs reactive power.

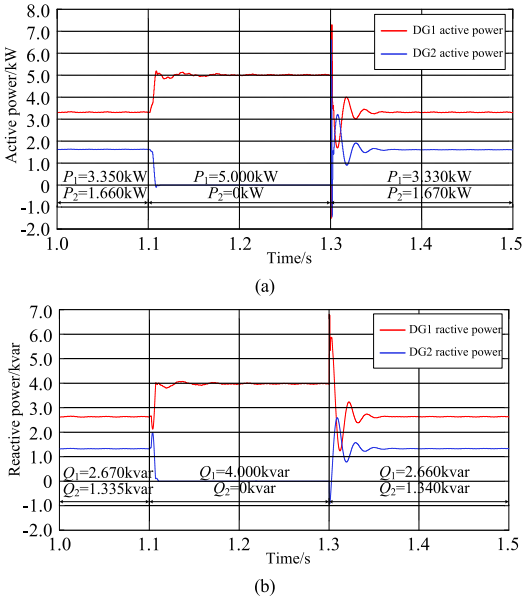

FIGURE 13. Simulation results under improved droop control strategy when DG switching. (a) DGs active power. (b) DGs reactive power.

TABLE 10. Comparison of voltage deviation ratio between traditional strategy and improved strategy when line parameters mutation.

Distributed generation	Active power deviation / %		Reactive power deviation / %	
	Traditional	Improved	Traditional	Improved
1	4.20	0.24	10.21	0.50
2	5.58	0.30	18.75	1.00

proposed control strategy. The motor load power demand is $P = 5$ kW, $Q = 4$ kvar, and the accurate allocation of active and reactive power is ensured. When $t = 1.1$ s, DG2 is

TABLE 11. Power allocation error of improved droop control strategy when switching on distributed generations.

Operation time / s	Active power allocation error / %	Reactive power allocation error / %
1.0-1.1	0.15	0.15
1.1-1.3	0	0
1.3-1.5	0.09	0.23

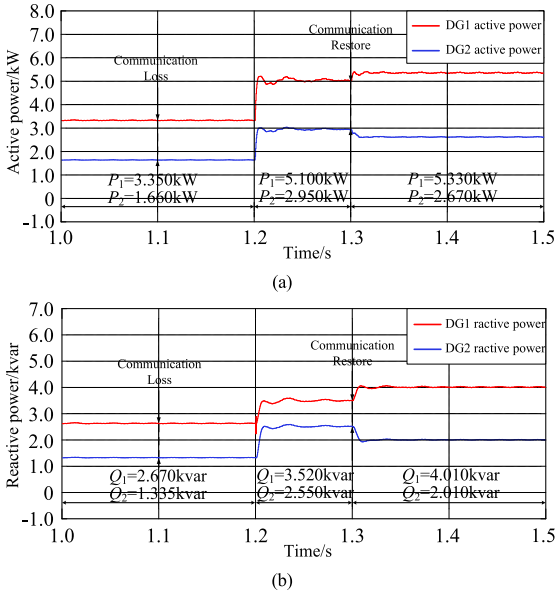

FIGURE 14. Simulation results under improved droop control strategy when communication link failure. (a) DGs active power. (b) DGs reactive power.

separated from the microgrid system and the output power of DG2 rapidly reduces to zero. Then, the DG1 provides the required power to the load and reaches a new stable point. At $t = 1.3$ s, DG2 is reintegrated into the system. After a short transient process, the system is re-stabilized and the plug-and-play functionality of multiple DGs is implemented.

Table 11 shows that the improved control strategy can accurately allocate the system power in the case of DG2 switching compared with the traditional droop control Therefore, it can be concluded that even in the case of a DG failure, the proposed control method can ensure that active and reactive power are allocated accurately according to each DG rated power.

5) COMMUNICATION LINK FAILURE

In order to verify the power allocation performance of the proposed method in the case of communication interruption, the communication system is cut off during 1.1 s to 1.3 s, and Fig. 14 shows the active and reactive power conditions in the process under the motor load. As mentioned earlier, once the local controller detects a communication failure, the droop coefficients k_P and k_Q will stop updating and remain at the final adjustment value. Therefore, even if communication is

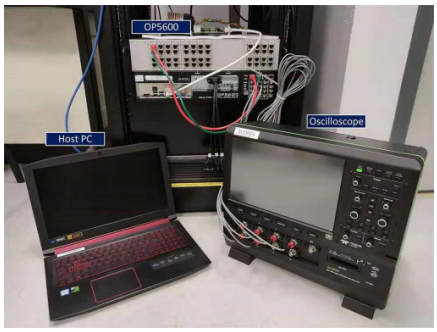

FIGURE 15. Experimental platform with hardware in loop based on RT-LAB.

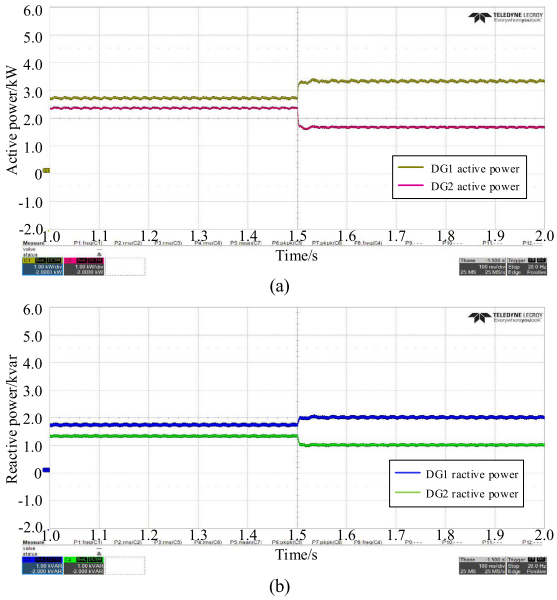

FIGURE 16. Experimental results before and after improved droop control is applied. (a) DGs active power. (b) DGs reactive power.

interrupted at $t = 1.1$ s, if the load does not change, the output power remains unchanged; when the load changes, it will cause an error in the power allocation accuracy between two DGs, but the error at this time is smaller than the traditional droop control. After $t = 1.3$ s communication recovery, the power allocation of the DG returns to its original accuracy.

Table 12 shows the allocation error of active and reactive power before and after communication interruption. It can be seen that although the power allocation accuracy is degraded due to communication system failure, the error is still much smaller than that of the traditional droop control. Therefore, the proposed algorithm can effectively response to the temporary interruption of the communication system.

In summary, compared with the traditional droop control, the improved droop control strategy proposed in this paper can achieve accurate power allocation under different operation conditions while maintaining the stability of the bus voltage and system frequency, and furthermore improve the dynamic performance and transient stability of the system.

TABLE 12. Power allocation error of improved droop control strategy in communication system failure.

Operation time / s	Active power allocation error / %	Reactive power allocation error / %
1.0-1.2	0.51	0.15
1.2-1.3	2.00	12.00
1.3-1.5	0.056	0.25

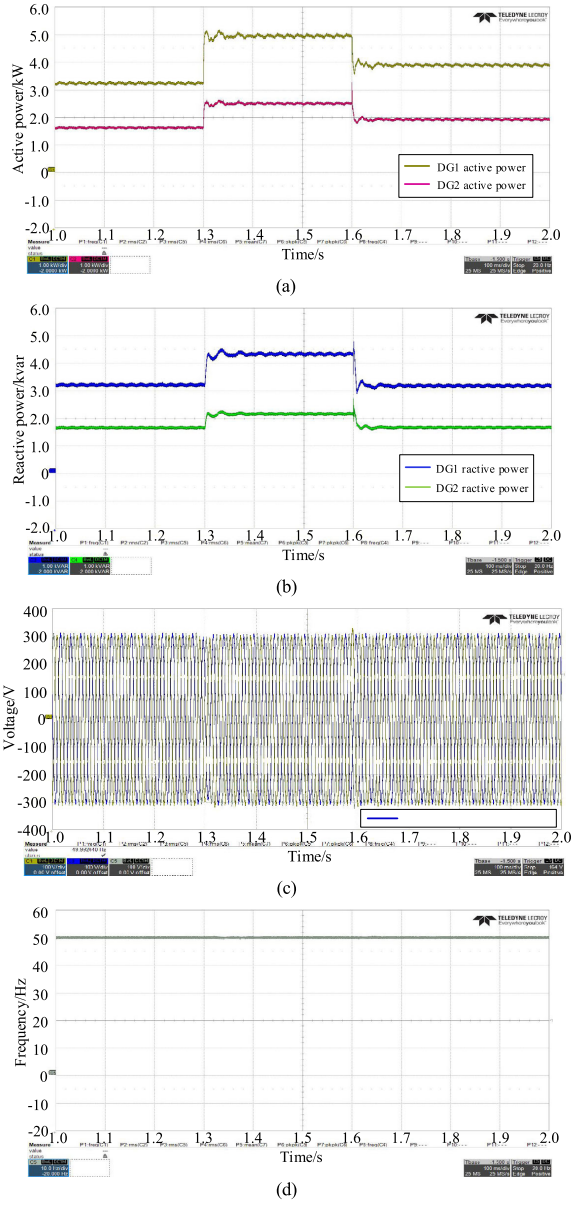

FIGURE 17. Experiment results under improved droop control strategy when motor load switching. (a) DGs active power. (b) DGs reactive power. (c) Bus voltage rms. (d) System frequency.

VI. EXPERIMENT RESULTS

In order to further verify the effectiveness of the proposed control strategy, a hardware-in-the-loop experiment based on RT-LAB real-time simulation platform was built. The host computer built the main circuit part. The control program was written in the control board, and the output I/O port was utilized by the oscilloscope to observe the waveform. The experimental platform is shown in Fig. 15. The system parameters are the same as the simulation platform, and the experimental waveform is shown in Fig. 16 and Fig. 17.

Fig. 16 illustrates the power allocation before and after the improved droop control is applied. Initially, DG used traditional droop control to power public loads. Due to the difference in line parameters, the active and reactive power allocation is inaccurate. Then, the algorithm proposed in this paper is put into $t = 1.5$ s to adjust the power allocation error. After an adjustment time of 0.3 s, the power allocation ratio of the two DGs is 2:1, which is consistent with its rated capacity.

Fig. 17 shows the experimental results when the system performs load switching and parameter changes under improved droop control strategy. The motor load was switched on and off at $t = 1.3$ s and 1.7 s, respectively, and at $t = 1.7$ s, the line parameters changed abruptly as in the simulation above. The results show that in the whole process, the active and reactive power can achieve a good allocation effect, while maintaining the stability of the bus voltage and frequency.

VII. CONCLUSION

In this paper, an improved droop control strategy based on improved particle swarm optimization in islanded microgrid with multiple distributed generations paralleled is proposed. By introducing fuzzy inference system to dynamically adjust the parameters of particle swarm optimization algorithm, the convergence speed and optimization precision of the original algorithm are improved. Then, the algorithm is used to optimize the traditional droop coefficient in real time, and the system is analyzed for small signal stability. Simulation and experimental results show that the control strategy can significantly improve the accuracy of power allocation while maintaining the stability of the bus voltage and system frequency, and realize the undifferential adjustment of voltage and power under different operating conditions, which effectively enhance the dynamic performance and transient stability of the system.

This paper only considers the case of two equivalent DGs in parallel. In the following work, the author will further study the microgrid with multiple DGs, and comprehensively consider the output characteristics of various DGs and improve the algorithm to enhance the performance of the proposed control strategy in more complex experimental environments.

REFERENCES

[1] S. Parhizi, H. Lotfi, A. Khodaei, and S. Bahramirad, "State of the art in research on microgrids: A review," *IEEE Access*, vol. 3, pp. 890–925, Jun. 2015.
[2] F. Nejabatkhah, Y. W. Li, and H. Tian, "Power quality control of smart hybrid AC/DC microgrids: An overview," *IEEE Access*, vol. 7, pp. 52295–52318, Apr. 2019.
[3] C. Wang, Z. Wu, and P. Li, "Research on key technologies of microgrid," *Trans. China Electrotech. Soc.*, vol. 29, no. 2, pp. 1–12, 2014.
[4] T. L. Vandoorn, J. D. M. De Kooning, B. Meersman, and Y. L. Vandevelde, "Review of primary control strategies for islanded microgrids with power-electronic interfaces," *Renew. Sustain. Energy Rev.*, vol. 19, pp. 613–628, Mar. 2013.

[5] S. Xu, W. Cao, and J. F. Zhao, "An integrated control strategy of the stabilization operation and mode smooth transfer for microgrids," *Trans. China Electrotech. Soc.*, vol. 33, no. 16, pp. 3855–3867, Aug. 2018.

[6] T. Morstyn, B. Hredzak, and V. G. Agelidis, "Control strategies for microgrids with distributed energy storage systems: An overview," *IEEE Trans. Smart Grid*, vol. 9, no. 4, pp. 3652–3666, Jul. 2018.

[7] Y. Han, H. Li, P. Shen, E. A. A. Coelho, and J. M. Guerrero, "Review of active and reactive power sharing strategies in hierarchical controlled microgrids," *IEEE Trans. Power Electron.*, vol. 32, no. 3, pp. 2427–2451, Mar. 2017.

[8] J. Yang, X. M. Jin, X. L. Yang, and X. Z. Wu, "Overview on power control technologies in hybrid AC-DC microgrid," *Power Syst. Technol.*, vol. 41, no. 1, pp. 29–39, Jan. 2017.

[9] Z. W. Liu, S. H. Miao, Z. H. Fan, K. Y. Chao, and Y. L. Kang, "Accurate power allocation and zero steady-state error voltage control of the islanding DC microgird based on adaptive droop characteristics," *Trans. China Electrotech. Soc.*, vol. 34, no. 4, pp. 795–806, Feb. 2019.

[10] J. He, Y. W. Li, and F. Blaabjerg, "An enhanced islanding microgrid reactive power, imbalance power, and harmonic power sharing scheme," *IEEE Trans. Power Electron.*, vol. 30, no. 6, pp. 3389–3401, Jun. 2015.

[11] Y. Hu, J. Xiang, Y. Peng, P. Yang, and W. Wei, "Decentralised control for reactive power sharing using adaptive virtual impedance," *IET Gener., Transmiss. Distrib.*, vol. 12, no. 5, pp. 1198–1205, Mar. 2018.

[12] J. Y. Zhang, J. Shu, J. Ning, L. Huang, and H. Wang, "Enhanced proportional power sharing strategy based on adaptive virtual impedance in low-voltage networked microgrid," *IET Gener., Transmiss. Distrib.*, vol. 12, no. 11, pp. 2566–2576, Jun. 2018.

[13] H. Zhang, S. Kim, Q. Sun, and J. Zhou, "Distributed adaptive virtual impedance control for accurate reactive power sharing based on consensus control in microgrids," *IEEE Trans. Smart Grid*, vol. 8, no. 4, pp. 1749–1761, Jul. 2017.

[14] Z. P. Lyu, M. Wu, H. Huang, C. M. Tu, Z. H. Song, and T. Zhao, "An improved droop control with network self-adaptability for distributed generation," *Power Syst. Technol.*, vol. 42, no. 9, pp. 2948–2957, Sep. 2018.

[15] M. A. Abdelwahed and E. F. El-Saadany, "Power sharing control strategy of multiterminal VSC-HVDC transmission systems utilizing adaptive voltage droop," *IEEE Trans. Sustain. Energy*, vol. 8, no. 2, pp. 605–615, Apr. 2017.

[16] J. C. Zhang, X. S. Wang, and L. Y. Ma, "An optimal power allocation scheme of microgrid using grey wolf optimizer," *IEEE Access*, vol. 7, pp. 137608–137619, Sep. 2019.

[17] Y. Mi, H. Y. Cai, Y. Y. Song, and Z. K. Li, "Study on reactive power sharing of island microgrid based on synchronous compensation," *Trans. China Electrotech. Soc.*, vol. 34, no. 9, pp. 1934–1943, May 2019.

[18] B. Y. Xu, H. B. Xu, Y. L. Zhao, H. T. Ge, K. Peng, and Z. H. Zhang, "Control principle and verification of constant-frequency synchronous current phasor based control strategy for Islanded microgrids," *Autom. Electr. Power Syst.*, vol. 43, no. 15, pp. 132–138, Aug. 2019.

[19] R. Pérez-Ibacache, A. Yazdani, C. Silva, and J. C. Agüero, "Decentralized unified control for inverter-based AC microgrids subject to voltage constraints," *IEEE Access*, vol. 7, pp. 157318–157329, Oct. 2019.

[20] J. Liu, Y. Miura, and T. Ise, "Comparison of dynamic characteristics between virtual synchronous generator and droop control in inverter-based distributed generators," *IEEE Trans. Power Electron.*, vol. 31, no. 5, pp. 3600–3611, May 2016.

[21] N. Soni, S. Doolla, and M. C. Chandorkar, "Inertia design methods for islanded microgrids having static and rotating energy sources," *IEEE Trans. Ind. Appl.*, vol. 52, no. 6, pp. 5165–5174, Nov./Dec. 2016.

[22] J. Liu, Y. Miura, H. Bevrani, and T. Ise, "Enhanced virtual synchronous generator control for parallel inverters in microgrids," *IEEE Trans. Smart Grid*, vol. 8, no. 5, pp. 2268–2277, Sep. 2017.

[23] Z. S. Peng, J. Wang, Y. T. Wen, D. Q. Bi, Y. X. Dai, and Y. Ning, "Virtual synchronous generator control strategy incorporating improved governor control and coupling compensation for AC microgrid," *IET Power Electron.*, vol. 12, no. 6, pp. 1455–1461, Jun. 2019.

[24] J. Li, B. Y. Wen, and H. Y. Wang, "Adaptive virtual inertia control strategy of vsg for micro-grid based on improved bang-bang control strategy," *IEEE Access*, vol. 7, pp. 39509–39514, Mar. 2019.

[25] J. Y. Zhang, J. Shu, J. Ning, and H. Wang, "Coordinated control for pv/storage hybrid islanded microgrid considering SOC balancing," *Trans. China Electrotech. Soc.*, vol. 33, no. S2, pp. 527–537, Dec. 2018.

[26] Q. F. Wu, X. F. Sun, Y. C. Hao, L. Qi, and Y. Cai, "Research of SOC balance and voltage frequence recovery of microgrid energy storage system," *Acta Energiae Sol. Sinica*, vol. 39, no. 6, pp. 1743–1751, Jun. 2018.

[27] C. Andalib-Bin-Karim, X. Liang, and H. Zhang, "Fuzzy-secondary-controller-based virtual synchronous generator control scheme for interfacing inverters of renewable distributed generation in microgrids," *IEEE Trans. Ind. Appl.*, vol. 54, no. 2, pp. 1047–1061,

[28] F. Valdez, P. Melin, and O. Castillo, "An improved evolutionary method with fuzzy logic for combining particle swarm optimization and genetic algorithms," *Appl. Soft Comput.*, vol. 11, no. 2, pp. 2625–2632, Mar. 2011.

[29] W. Q. Xie, M. X. Han, H. J. Wang, R. Li, and M. Wu, "Multi-source coordinated control strategy of DC micro-grid based on virtual voltage," *Proc. CSEE*, vol. 38, no. 5, pp. 1408–1418, Mar. 2018.

[30] F. Guo, C. Wen, J. Mao, J. Chen, and Y.-D. Song, "Distributed cooperative secondary control for voltage unbalance compensation in an islanded microgrid," *IEEE Trans. Ind. Informat.*, vol. 11, no. 5, pp. 1078–1088, Oct. 2015.

[31] K. Yu, Q. Ai, S. Wang, J. Ni, and T. Lv, "Analysis and optimization of droop controller for microgrid system based on small-signal dynamic model," *IEEE Trans. Smart Grid*, vol. 7, no. 2, pp. 695–705, Mar. 2016.

[32] X. Z. Liu, J. L. Wen, Y. Pan, P. F. Wu, and J. Y. Li, "OPF control of DC-grid using improved PSO algorithm," *Power Syst. Technol.*, vol. 41, no. 3, pp. 715–720, Mar. 2017.

[33] Z. S. Peng, J. Wang, D. Q. Bi, Y. T. Wen, Y. X. Dai, X. Yin, and Z. J. Shen, "Droop control strategy incorporating coupling compensation and virtual impedance for microgrid application," *IEEE Trans. Energy Convers.*, vol. 34, no. 1, pp. 277–291, Mar. 2019.

[34] M. B. Shafik, H. K. Chen, G. I. Rashed, R. A. El-Sehiemy, M. R. Elkadeem, and S. R. Wang, "Adequate topology for efficient energy resources utilization of active distribution networks equipped with soft open points," *IEEE Access*, vol. 7, pp. 99003–99016, Jul. 2019.

[35] A. Milczarek, M. Malinowski, and J. M. Guerrero, "Reactive power management in islanded microgrid-proportional power sharing in hierarchical droop control," *IEEE Trans. Smart Grid*, vol. 6, no. 4, pp. 1631–1638, Jul. 2015.

[36] X. Y. Li, J. P. Zhou, H. Q. Li, T. Wang, W. Z. Zhang, and D. J. Mao, "Improved droop control strategy for real-time power sharing of microgrid based on particle swarm optimization," *High Voltage Eng.*, vol. 44, no. 10, pp. 3425–3432, Oct. 2018.

[37] P. Melin, F. Olivas, O. Castillo, F. Valdez, J. Soria, and M. Valdez, "Optimal design of fuzzy classification systems using PSO with dynamic parameter adaptation through fuzzy logic," *Expert Syst. Appl.*, vol. 40, no. 8, pp. 3196–3206, Jun. 2013.

[38] S. X. Cheng, H. Zhan, and Z. X. Shu, "An innovative hybrid multi-objective particle swarm optimization with or without constraints handling," *Appl. Soft Comput.*, vol. 47, pp. 370–388, Oct. 2016.

[39] Q. Feng, Q. Li, P. Chen, H. Wang, Z. Xue, L. Yin, and C. Ge, "Multi-objective particle swarm optimization algorithm based on adaptive angle division," *IEEE Access*, vol. 7, pp. 87916–87930, Jun. 2019.

[40] X. Yu, X. She, X. Ni, and A. Q. Huang, "System integration and hierarchical power management strategy for a solid-state transformer interfaced microgrid system," *IEEE Trans. Power Electron.*, vol. 29, no. 8, pp. 4414–4425, Aug. 2014.

[41] S. Y. Altahir, X. W. Yan, and A. S. Gadalla, "Active and reactive power sharing control strategy for VSGs in microgrid considering the different capacities of distributed energy resources," *IET Cyber-Phys. Syst., Theory Appl.*, vol. 3, no. 3, pp. 167–173, Oct. 2018.

[42] T. C. Deng, X. W. Yan, Y. F. Cheng, T. Q. Hua, W. C. Zhang, and Y. Zhang, "Circulating-current analysis and power distribution control of parallel inverters with different power ratings in microgrid," *Southern Power Syst. Technol.*, vol. 11, no. 1, pp. 58–64, Feb. 2017.

[43] J. Kim, J. M. Guerrero, P. Rodriguez, R. Teodorescu, and K. Nam, "Mode adaptive droop control with virtual output impedances for an inverter-based flexible AC microgrid," *IEEE Trans. Power Electron.*, vol. 26, no. 3, pp. 689–701, Mar. 2011.

[44] M. R. Zhang, Z. C. Du, and S. B. Wang, "Research on droop control strategy and parameters selection of microgrids," *Trans. China Electrotech. Soc.*, vol. 29, no. 2, pp. 136–144, Feb. 2014.

[45] *IEEE Standard for Interconnection and Interoperability of Distributed Energy Resources With Associated Electric Power Systems Interfaces*, IEEE Standard 1547-2018 (Revision of IEEE Standard 1547-2003), Apr. 2018, pp. 1–138.

[46] X. Li, C. Liu, S. Wu, S. Chi, and P. C. Loh, "Sliding-mode flux-weakening control with only single current regulator for permanent magnet synchronous motor," *IEEE Access*, vol. 7, pp. 131616–131626, Jul. 2019.
[47] E.-K. Kim, J. Kim, H. T. Ngyuen, H. H. Choi, and J.-W. Jung, "Compensation of parameter uncertainty using an adaptive sliding mode control strategy for an interior permanent magnet synchronous motor drive," *IEEE Access*, vol. 7, pp. 11913–11923, Jan. 2019.

LIANG ZHANG received the B.Sc. degree from the Hebei University of Science and Technology, China, in 2007, and the M.S. and Ph.D. degrees in electrical engineering and automation from the Harbin Institute of Technology, Harbin, China, in 2010 and 2015, respectively. He was a Visiting Ph.D. Student with The University of British Columbia, Vancouver, BC, Canada, in 2014. He is currently an Associate Professor with the Department of Electrical Engineering, Northeast Electric Power University, China. His current research interests include ac/dc hybrid microgrids, V2G communication, vehicular communication, the energy Internet, and power line communication.

HAO ZHENG received the B.S. degree from the Qufu Normal University, China, in 2018. He is currently pursuing the M.S. degree in electrical engineering with Northeast Electric Power University, Jilin, China. His main interests and research field are microgrid operation and control.

QUANGUI HU graduated from the Jiangxi University of Finance and Economics, in 2005, where he is currently the Chief Engineer of the Beijing SGITG Accenture Information Technology Center Company, Ltd., where mainly focuses on grid information technology research, and the energy Internet advanced technology.

BIN SU graduated from the Electrical Engineering Department, North China Electric Power University, in 2000. She is currently the Deputy Director and an Engineer of the Finance Consulting Business Center, Beijing SGITG Accenture Information Technology Center Company, Ltd. She mainly focuses on the research of power grid information technology, the power Internet finance, and FICO.

LING LYU received the M.S. degree in control science and engineering from Yanshan University, Qinhuang, China. She is currently working as an Experimenter with Northeast Electric Power University, Jilin, China. Her main research fields are V2G and microgrid technology.